Compositional dependence of local atomic structures in amorphous $Fe_{100-x}B_x$ ($x=14,17,20$) alloys studied by electron diffraction and high-resolution electron microscopy

Akihiko Hirata,[1,*] Yoshihiko Hirotsu,[1] Tadakatsu Ohkubo,[1,†] Takeshi Hanada,[1] and V. Z. Bengus[2]

[1]*The Institute of Scientific and Industrial Research, Osaka University, 8-1 Mihogaoka, Ibaraki, Osaka 567, Japan*
[2]*The B. Verkin Institute for Low-Temperature Physics and Engineering of Academy of Science of Ukraine, Kharkov-164 310164, Ukraine*

Local atomic structures of rapidly quenched amorphous $Fe_{100-x}B_x$ ($x=14,17,20$) alloys have been investigated comprehensively by means of high-resolution electron microscopy (HREM), nanobeam electron diffraction (NBED), and electron diffraction atomic pair distribution function (PDF) analysis. In HREM images, crystalline cluster regions with a bcc-Fe structure extending as small as 1 nm were observed locally as lattice images, while NBED with a probe size as small as 1 nm revealed an existence of local clusters with structures of bcc-Fe and also of Fe-boride in all the as-formed alloys. Atomic PDF analyses were performed for these alloys by precise measurements of halo-electron diffraction intensities using imaging-plate and energy-filtering techniques. From the interference functions, atomic structure models were constructed for the Fe-B amorphous structures with the help of reverse Monte Carlo calculation. From Voronoi polyhedral analysis applied to these structure models, it was confirmed that atomic polyhedral arrangements with bcc and icosahedral clusters of Fe, and trigonal prisms of Fe and B, are formed in these amorphous structures, and the fraction of bcc-Fe clusters increases with the Fe content, while the fraction of trigonal prisms increases with the B content. The direct observation of local cluster structures of bcc-Fe and Fe-boride by HREM and NBED is an indication of "nanoscale phase separation" driven in the course of amorphous formation of these alloys, and the constructed structures based on the experimental PDFs with different B contents are inconsistent with a local structure scheme expected from the "nanoscale phase separation" model. The present study demonstrates that the structure model of nanoscale phase separation stands for the amorphous alloy structures where the phase separation fatally occurs in the crystallization stage.

I. INTRODUCTION

Recently, bulk metallic glasses (BMGs)[1,2] of metal-metal and metal-metalloid multicomponent systems with clear glass-transition temperatures have been attracting much interest, and in these glasses local atomic arrangements are considered to play an important role for the stabilization of glass phases. Detailed investigations of local atomic arrangements in metallic glasses of multicomponent systems are now becoming important.[3] However, local atomic arrangements of metallic glasses (amorphous alloys) even in binary systems are still not understood in detail.

A number of x-ray and neutron diffraction structure analyses have been performed for binary amorphous alloys with transition metal-metalloid (TM-M) systems such as Fe-B and Pd-Si. Atomic short-range order (SRO) with respect to the nearest-neighbor structures has been studied, and for the TM-M systems it is generally accepted that the SRO structure stabilizing the TM-M amorphous structures is the trigonal-prism-related structural network without a long-range correlation in the network formation.[4–7] Connectivity and its spatial extension of these trigonal-prism structural units form a kind of medium-range order (MRO) structure in the TM-M amorphous structure.[8–10] Structure analyses in these studies are based on the averaged-homogeneous structure concept. Within the concept, we can argue local SRO and MRO structures. On the other hand, Hamada and Fujita[11] proposed a "crystal-embryo model" for the amorphous Fe-B structure, where bcc-Fe clusters are formed in the

amorphous matrix during quenching from the melt. Dubois and Le Caer[12] also proposed a "microphase separation model" for the amorphous structures of Fe-B and Pd-Si. (Note that the term "phase separation" is nowadays often used for such a phase separation phenomenon as "spinodal decomposition;" however, the term basically covers both of the phase separation phenomena as "precipitate type" and "spinodal type.")

In this model, amorphous structures are locally decomposed into nanoscale phases with the phase valence depending on their compositions. Local nanoscale crystalline phases (nanoclusters) in this model cannot be taken as nuclei in crystallization but can be taken as extended MRO structures when their sizes are below the critical sizes for nucleation. The above structure models belong to inhomogeneous structure models, which can explain the experimental data of Mössbauer spectroscopy,[11–13] thermomagnetization,[14] and crystallization enthalpy[15] satisfactorily. In this sense, these are realistic structure models. In spite of these proposals of glass structure of TM-M systems, no detailed examination of the structural model has been done on an atomic structure level even in simple binary TM-M systems.

For the purpose of imaging of local structures of TM-M amorphous alloys, we have made high-resolution electron microscopy (HREM) studies of the alloys with eutectic compositions. In an a-$Fe_{84}B_{16}$ (hereafter, "a-" denotes "amorphous") ribbon specimen, local crossed-lattice fringe images extending as small as 1 nm were observed corresponding to locally ordered regions with a bcc-Fe(B) structure (B was

presumed to be dissolved in the structure) under a suitable defocus condition[16] in spite of appearance of a halo pattern in electron diffraction. Using the same technique, we also observed locally ordered regions with the fcc-Pd(Si) structure in a-Pd$_{77.5}$Cu$_6$Si$_{16.5}$ (ribbon)[17] and a-Pd$_{82}$Si$_{18}$ (film,[18] ribbon[19]) alloys. In the study of a-Pd$_{82}$Si$_{18}$ structure, nanobeam electron diffraction (NBED) directly identified the fcc-Pd(Si) clusters.[20] These studies demonstrated that amorphous TM-M alloys with near-eutectic compositions have locally ordered structures in the form of α-phase (with bcc or fcc-structures) atomic structures. Such a structural feature with locally ordered regions is observed rather commonly in amorphous alloys.[21,22]

As already explained, x-ray and neutron diffraction studies found local SRO or MRO structures with trigonal prisms in TM-M amorphous alloys, while magnetic and HREM studies found nanoclusters with the α-phase atomic structure in the amorphous alloys. In order to explain the above discrepancy on the local structures, we have recently studied local structures of a-Pd$_{82}$Si$_{18}$ more in detail on the basis of electron microscopy and electron diffraction structure analysis[20] by introducing a structural model of "nanoscale phase separation," which is as same as the structure concept proposed by Hamada-Fujita[11] and Dubois-Le Caer.[12] In this structure model, α-phase clusters corresponding to those of the α-phase structure were homogeneously distributed and embedded in the metalloid-enriched amorphous matrix which was composed of a dense-randomly packed (DRP) structure of Pd and Si. A suitable structure model with fcc-Pd(Si) clusters (about 10 vol %.) embedded in a DRP structure of Pd and Si with the trigonal SRO structures was finally obtained for this amorphous alloy with the help of reverse Monte Carlo (RMC) simulation,[23,24] which could explain the experimental atomic pair distribution function (PDF) from electron diffraction and also HREM images quite satisfactorily. From this study, it was demonstrated that such a structure with "nanoscale phase separation" is thought to be a quenched-in nonequilibrium structure of amorphous alloys directing to a development of phase separation, which fatally occurs in their crystallization stages on annealing.

In order to confirm a general adaptability of the structure model of nanoscale phase separation to amorphous alloys of TM-M systems, it is important to know compositional dependence of local atomic structures of the as-formed TM-M amorphous alloys with different compositions. The present study has been performed to know local atomic structures of the as-formed amorphous Fe-B alloys with different compositions to establish the structural model of nanoscale phase separation. For this, we took advantage of electron diffraction structure analysis together with the HREM observation and nanobeam electron diffraction (NBED) for local structure studies. It should be noted that electron diffraction has an advantage to obtain scattering information from the same specimen area as used for HREM and NBED, and the scattering information is from a wide special frequency range in addition to the strong scattering from light atoms. Selected area electron diffraction (SAED) patterns were taken using a transmission electron microscope (TEM) equipped with an energy filter. The elastically scattered electron intensities were recorded on imaging plates (IPs) for a precise measurement of electron intensity profiles for the PDF analysis. Atomic structure models were constructed in computer using RMC calculation followed by a Voronoi polyhedral analysis for their local structures.

II. EXPERIMENTAL PROCEDURES

A. Specimens and structural observation

Amorphous specimens of Fe$_{100-x}$B$_x$ ($x = 14, 17$, and 20) were prepared in the form of ribbons with a thickness of 30 μm and a width of 6 mm by rapid quenching. The B compositions of the specimens were determined by plasma optical spectroscopy. For TEM and electron diffraction studies, the ribbon specimens were thinned by using both Ar-ion thinning and electrolytic polishing (with acetic and perchloric acids) techniques. Note that the results obtained from these different thinning techniques basically show the same image and diffraction features. In the ion thinning, a specimen stage capable of low glancing-angle ion thinning with a low voltage of 200 V was used in the final thinning. A HREM observation was made using a JEM-2010 TEM operating at 200 kV. Halo-diffraction intensities from the specimens were recorded on IP in a LEO-922D TEM equipped with an omega-type energy filter. For nanodiffraction, a field-emission type TEM (JEM-3000F) was used at 300 kV with an electron probe size as small as 1 nm. In order to make the beam convergence of nanoprobe as small as possible ($<1 \times 10^{-2}$ rad), the smallest condenser-lens aperture (hole diameter: 10 μm) was used. In recording the NBED patterns, a charge-coupled device (CCD) camera with a TV-rate was used.

B. PDF analysis from electron diffraction intensity

The energy filtering in electron diffraction was performed using an energy window with a width of ±10 eV. Diffraction intensity was measured in thin film specimen areas to avoid the multiple scattering. The thickness of the areas in electron diffraction were thinner about 10–20 nm, estimated from plasmon-loss spectrum in electron energy-loss spectroscopy (EELS). The diffraction intensity was recorded on an IP with a pixel size of 17.5×17.5 μm^2. The exposure times for the IP recording were 4 s and 69 s for low $Q(\sim 120$ nm$^{-1})$ and high $Q(\sim 180$ nm$^{-1})$ regions, respectively. The intensity $I(x,y)$ on the IP at (x,y) position was digitized using an IP reader (DITABIS-MICRON) on 65 536 gray levels. The intensities $I(x,y)$ at the same radial distance of R from the peak position of the direct spot were averaged. The averaged value $\langle I(x,y) \rangle$ for the common distance R was then read as the observed intensity $I_{obs}(Q)$ for the scattering vector Q using the relationship, $Q = 4\pi \sin \theta / \lambda = (2 \pi R / L\lambda)(1 - 3R^2/8L^2)$, where θ is the half scattering angle and λ the electron wave length. The camera length L was set at 256 mm but the length was corrected using a reference diffraction ring pattern from gold fine particles. From the observed elastic intensity $I_{obs}(Q)$, the interference function $i(Q)$ can be obtained by[9]
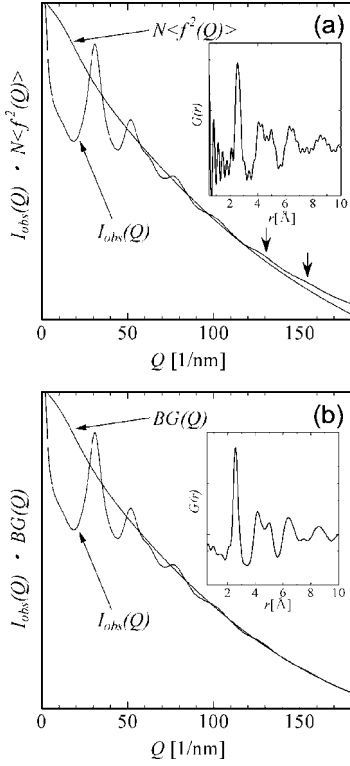
FIG. 1. Scattered intensity profiles obtained from the thin specimen areas along the $N\langle f^2(Q)\rangle$ (a) and $BG(Q)$ (b) curves, together with $G(r)$ curves.

$$i(Q) = \frac{I_{\text{obs}}(Q) - N\langle f^2(Q)\rangle}{N\langle f(Q)\rangle^2}. \qquad (1)$$

Here, Q is the scattering vector and N means atom number. The square-mean and mean-square atomic scattering factors are expressed as $\langle f^2(Q)\rangle = \Sigma N_j f_j^2(Q)/N^2$ and $\langle f\rangle^2 = [\Sigma N_j f_j(Q)]^2/N^2$, respectively. It should be noted that in a precise electron diffraction intensity analysis, the most important procedure is to obtain diffraction intensity profiles as close as that of kinematical intensity with less inelastic scattering and multiple scattering, and with good linearity in intensity recording. The scattered intensity profiles obtained from the thin specimen areas in this study varied almost along the $N\langle f^2(Q)\rangle$ curve, although the curve slightly deviates from the $I_{\text{obs}}(Q)$ at the high-Q region. We already checked that the slight deviation is mainly ascribed to a residual inelastic scattering. However, it is practically difficult to set the energy window less than 20 eV for the present purpose because of the design of the energy filter. This can be seen in Fig. 1(a) for the $I_{\text{obs}}(Q)$ profile together with $N\langle f^2(Q)\rangle$ for the a-Fe$_{80}$B$_{20}$ specimen. As is shown in figure, at a high-Q region, we can see slight oscillation in the $I_{\text{obs}}(Q)$ profile indicated by arrows. Note that the electron diffraction technique is advantageous to detect such oscillation at the high-Q region, and the imaging plate, used in this study, enables us to read very weak intensity due to its wide dynamic range. To precisely read the information of the slight oscillation, a slight modification of the background intensity is necessary in the following way. First, the $i(Q)$ can be

transformed to the total reduced pair distribution function as

$$G(r) = \frac{2}{\pi}\int_0^\infty Qi(Q)\sin(Qr)dQ = 4\pi r[\rho(r) - \rho_0], \qquad (2)$$

where $\rho(r)$ is the atomic density and ρ_0 the average atomic density that can be obtained from the specimen physical density. Note that the exact coordination numbers cannot be obtained from the $G(r)$ in the case of alloys. The $G(r)$ profile obtained from the Fourier transform of $Qi_{\text{obs}}(Q)$ using Eqs. (1) and (2) gives a ripple near $G(r)$ with $r\sim0$. This comes from the background intensity and cannot be drawn correctly, and therefore a redrawing is generally necessary in such a case.[25] In our electron diffraction study, we still have a possibility of small contributions from multiple or thermal scattering and also from recorded intensity noise, especially in the very weak intensity level in an IP recording. The calculation of the background intensity in this work was then made repeatedly so that the ripple near $r\sim0$ became minimized in the final $G(r)$ profile. The modified background intensity $BG(Q)$ is drawn in Fig. 1(b), together with a corresponding $G(r)$ profile where the ripple near $r\sim0$ is sufficiently reduced.

C. Reverse Monte Carlo simulation

Successful structure models must reproduce the shapes of the interference functions up to high-Q vector regions. The RMC simulation used in this study was able to satisfy the requirement. In the RMC procedure, we fitted a calculated total interference function $i_{\text{cal}}(Q)$ obtained from a structural model with the experimentally obtained $i_{\text{exp}}(Q)$. A detail of the structural model will be described later. The $i_{\text{cal}}(Q)$ was obtained as follows: (i) The partial pair distribution functions $g_{\text{cal}}^{ab}(r)$ were directly derived from the structural model, where the indices of a and b mean atomic species. (ii) Partial calculated interference functions $i_{\text{cal}}^{ab}(Q)$ were obtained by Fourier transform of $g_{\text{cal}}^{ab}(r)$. (iii) Total calculated interference function $i_{\text{cal}}(Q)$ was finally achieved by summing up $i_{\text{cal}}^{ab}(Q)W_{ab}$ for each pair. Here, W_{ab} means a weighting factor that is defined as $W_{ab} = x_a x_b f_a(Q)f_b(Q)/\langle f(Q)\rangle^2$ for each partial $i_{\text{cal}}^{ab}(Q)$, and can be calculated for each Q vector by knowing x_a and f_a, where x_a and f_a mean concentration and atomic scattering factor for an a atom. The fitting consists of choosing atoms at random and moving them in arbitrary directions with arbitrary amounts. An event of the atomic positional movement was accepted to be preferable if the move resulted in a decrease of the mean square deviation, χ^2, between $i_{\text{exp}}(Q)$ and $i_{\text{cal}}(Q)$ within the Q vector up to 180 nm^{-1}. Even if χ^2 increases, the atomic movement was accepted with a probability of $\exp[-(\chi^2_{\text{new}} - \chi^2_{\text{old}})/2]$. Otherwise, the movement was rejected. Here, χ^2 was defined as $\chi^2 = \Sigma[i_{\text{exp}}(Q) - i_{\text{cal}}(Q)]^2/\sigma(Q)$, where $\sigma(Q)$ is the experimental error. We here used a constant $\sigma(Q)$ value of 0.01, independent of Q-vectors. χ^2_{old} and χ^2_{new} mean χ^2 values before and after one event of atomic movement, respectively. The simulation was carried out using the RMCA program.[26] In the present simulation, initial structures for the three Fe-B specimens were
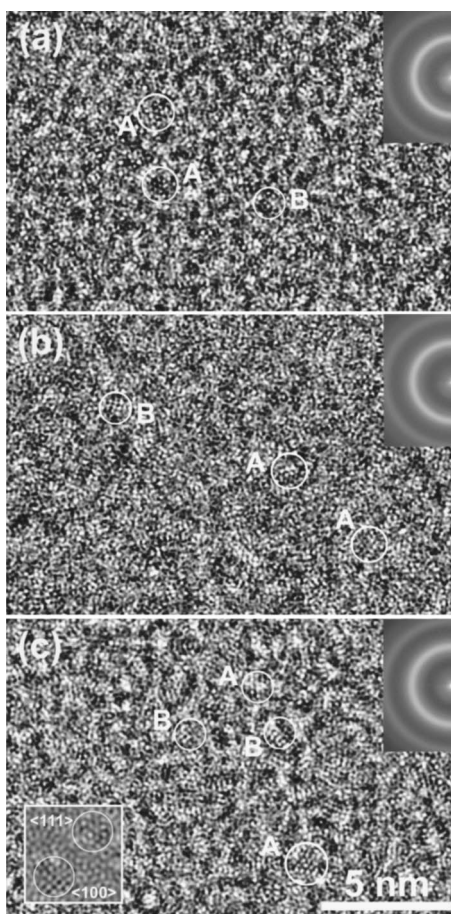
FIG. 2. HREM images of as-formed $Fe_{86}B_{14}$ (a), $Fe_{83}B_{17}$ (b), and $Fe_{80}B_{20}$ (c) amorphous alloys showing local crystalline cluster regions. Encircled regions lettered A and B are examples of $\langle 111 \rangle$ and $\langle 100 \rangle$ oriented bcc-Fe(B) cluster regions with crossed-lattice fringes having fringe spacings of ~0.20 nm. The simulated image with 60 nm underfocus is also shown in the inset.

random atomic structure models with three different compositions. In calculating, constraints concerning closest atomic distances were applied to satisfy the reported result where partial interference functions were experimentally determined by x-ray and neutron diffraction.[6] According to the report, there was no nearest B-B atomic pairs and the closest distance was 0.357 nm. Total atoms are 5000, independent of the composition, forming a cubic cell. The cell sizes are 3.81 nm^3 for a-$Fe_{86}B_{14}$, 3.79 nm^3 for a-$Fe_{83}B_{17}$, and 3.76 nm^3 for a-$Fe_{80}B_{20}$ according to their corresponding densities 7.41, 7.36, and 7.31 g/cm^3.

III. RESULTS AND DISCUSSION

A. Local structures studied by HREM and NBED

In our previous HREM study for the imaging of MRO structures in a-$Fe_{84}B_{16}$,[16] we observed bcc-Fe clusters as the MRO regions in the form of localized lattice fringe regions extending as small as $1-2$ nm under suitable defocused conditions. In the present study, we confirmed the formation of such MRO regions by HREM as shown in Fig. 2. The ob-

servation condition of the MRO regions was also based on the "defocus method,"[16,19] which enables lattice imaging of localized crystalline atomic clusters embedded in amorphous matrix considering the phase-contrast transfer function.[27] In Fig. 2, the spacing of the local lattice fringes was about 0.20 nm. In the figures, the clearly observed crossed-lattice fringe regions are extending about $1-2$ nm, although their images are often deformed due mainly to their atomic displacements in the clusters. It should be noted that in the a-$Fe_{86}B_{14}$ and a-$Fe_{83}B_{17}$ specimens, we frequently observed the crossed-lattice fringe regions with six- and fourfold symmetries resembling the $\langle 111 \rangle$ and $\langle 100 \rangle$ images of the bcc-clusters (denoted by A and B regions, respectively). Such images are also observed in a-$Fe_{80}B_{20}$ in Fig. 2(c). In SAED, halo patterns are observed from all the specimens, as seen in the insets in Fig. 2.

In order to confirm that the appearance of such six- and fourfold lattice fringe images in Fig. 2 is due to the local bcc-Fe(B) clusters, image simulations were conducted using an atomic Fe-B structure model. In the structure model, $\langle 111 \rangle$- and $\langle 001 \rangle$-oriented near-spherical bcc-Fe(B) clusters with a size of 1.3 nm in diameter were embedded in a DRP Fe-B structure. The cell size of the model was 3.0 nm $\times 3.0$ nm $\times 3.0$ nm, including 2031 Fe and 511 B atoms. The composition and atomic density of the model structure correspond to $Fe_{80}B_{20}$ and the experimental density of 7.31 g/cm^3, respectively. In the model, the bcc-clusters included B atoms at both the interstitial and substitutional sites formed by the bcc-Fe lattice, and the composition was chosen to be the same as the average composition $Fe_{80}B_{20}$. The image simulation was performed using a multislice technique[27] taking the multiple scattering into consideration. The simulated $\langle 111 \rangle$- and $\langle 001 \rangle$-oriented Fe(B) cluster images under the same defocused condition (60 nm underfocus) as used in taking all the images in Fig. 2 are shown in the inset in Fig. 2(c). The atom positions are in bright contrast under the defocus. It should be noted that the correspondence between the simulated and observed local lattice images is quite well, and that the observed local cluster images (such as images at A and B) are identified as bcc-Fe clusters.

Local lattice image features with lattice cross angles and fringe spacings different from those of the bcc-Fe clusters were not clearly observed in any of the three specimens. This seems to suggest the bcc-Fe clusters are formed predominantly in these Fe-B glasses, although iron-boride clusters are, in principle, also expected to be present as another component when we expect a nanoscale phase separation in the as-formed structures of these glasses. Therefore, NBED was further performed in this study to investigate the local structure in more detail. In taking NBED patterns, nanoareas were continuously scanned from site to site for about 30 min in the TV-rate recording for each specimen. Examples of NBED patterns are shown in Fig. 3, which were taken from the a-$Fe_{80}B_{20}$ alloy. $\langle 100 \rangle$ and $\langle 111 \rangle$ zone-axis patterns from bcc-Fe clusters are clearly seen in Figs. 3(a) and 3(b), respectively. Because of the possible lattice distortions in the bcc-clusters due to the B atom inclusion or a stress from the matrix, we cannot always expect right angles (90° or 60°) between the 110-type diffraction vectors. Diffraction spots as
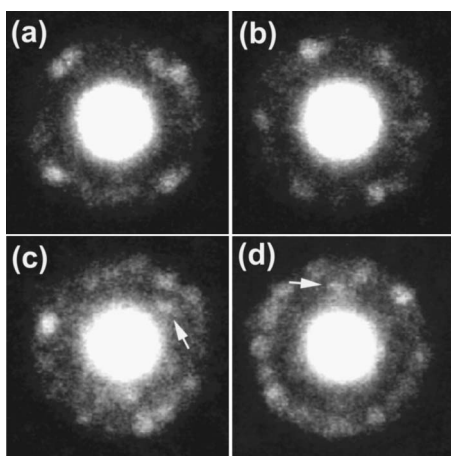
FIG. 3. NBED patterns from cluster regions in the as-formed $Fe_{80}B_{20}$ alloy. $\langle 100 \rangle$ (a) and $\langle 111 \rangle$ (b) zone-axis patterns from bcc-Fe(B) clusters are seen, while in (c) and (d) diffraction spots (indicated) from Fe-boride clusters are seen.
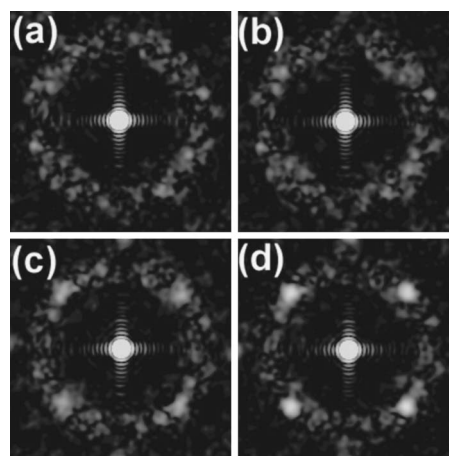

FIG. 4. Simulated NBED patterns obtained from the models of (a) dense random packing structure, and bcc-Fe cluster with a diameter of (b) 1 nm, (c) 1.5 nm, and (d) 2 nm embedded in dense random packing structure.

indicated by arrows in Figs. 3(c) and 3(d) with an interplanar spacing of about 0.25 nm are sometimes observed from the specimen, which are presumably from Fe-boride clusters. There are several interplanar spacings close to 0.25 nm with strong scattering intensities in Fe_3B and Fe_2B, though their atomic structures are supposed to be deformed in such nanophase clusters with sizes smaller than 1 nm. NBED patterns from the a-$Fe_{86}B_{14}$ and a-$Fe_{83}B_{17}$ specimens gave almost the same results as obtained from a-$Fe_{80}B_{20}$. In the nanodiffraction patterns in Fig. 3, we also observe weak diffraction spots forming the circle corresponding to the first halo-diffraction ring in SAED. These diffuse spots are considered to come from coherently scattered electrons, scattered from the disordered matrix atoms. It was found that the chance of observing such clear diffraction spots from the second-phase nanoclusters as seen in Figs. 2(c) and 2(d) is small in contrast to a rather high chance of observing diffraction spots from bcc-Fe clusters. In other words, the Fe-boride clusters with the size of about 1 nm are formed locally but their formation is not frequent in these Fe-based glasses.

To confirm the presence of the bcc-Fe clusters in the amorphous states, we performed computer calculation concerning the NBED patterns[28] from the appropriate structural model, including the bcc-Fe clusters. Figure 4 shows the simulated NBED patterns obtained from a DRP structure model with no bcc-Fe cluster in Fig. 4(a), and the other three models including bcc-Fe cluster with a diameter of 1 nm in Fig. 4(b), 1.5 nm in Fig. 4(c), and 2.0 nm in Fig. 4(d). The structure models contain 5000 atoms (4000 Fe atoms and 1000 B atoms) in the cubic cells. The simulation was performed by assuming the nanobeam probe with a full width at half maximum (FWHM) of 1 nm. The simulated NBED of 1.5 nm model well reproduces the experimental one. From this result, we confirmed the existence of the bcc-Fe cluster with a diameter as small as about 1.5 nm in the DRP amorphous matrix.

B. RMC-simulated structures and atomic correlations

From Figs. 2 and 3, it has been demonstrated that similar to the case of a-Pd-Si,[20] the nanoscale phase separation (de-

composition) must be occurring in the present a-Fe-B alloys. We then became interested in whether there is a compositional dependence of observation frequency of bcc-Fe clusters (or Fe-boride clusters) reflecting the "phase rule" in thermodynamics or not. In the HREM and NBED studies, however, it was hard to obtain such statistical structural information. In order to confirm the nanoscale phase separation in the as-formed Fe-B alloys, it is quite important to obtain composition-dependent local structure information by other experimental methods. According to our previous structural work,[20] electron diffraction structure analysis from the same specimens used for HREM and NBED studies, followed by the reverse Monte Carlo structure simulations and Voronoi polyhedral analysis would be able to contribute to the demonstration of it.

Figure 5 shows the $i_{obs}(Q)$ profiles (solid lines) obtained from the a-$Fe_{86}B_{14}$, a-$Fe_{83}B_{17}$, and a-$Fe_{80}B_{20}$ specimens. These profiles were obtained from the elastic $i_{obs}(Q)$ profiles up to a high-Q vector as large as 180 nm^{-1}. A small difference between the $i_{obs}(Q)$ profiles is found at or near the first and the second intensity peaks. The calculated $i_{cal}(Q)$ profiles are also shown as open circles fitted to the experimental profiles. The fitting was performed to the experimental $i_{obs}(Q)$ in the Q range of 20–180 nm^{-1}. As shown in the figures, the correspondence is very well for each specimen.

In Figs. 6(a)–6(c), the results of simulated PDFs obtained from the Fourier transform of RMC-simulated final $i_{cal}(Q)$ profiles for a-$Fe_{86}B_{14}$, a-$Fe_{83}B_{17}$, and a-$Fe_{80}B_{20}$ are shown, respectively. In the figures, the total and the partial PDFs are drawn. From the atomic partial PDF profiles in the RMC-simulated structure, we can calculate partial atomic coordination numbers for central Fe and B atoms (for Fe-Fe, Fe-B, and B-Fe correlations) in each specimen. This was performed by integrating the first correlation peaks for the atomic pairs of Fe-B and Fe-Fe with peak positions at about 0.21 and 0.25 nm, respectively. In Table I, the obtained atomic coordination numbers are shown together with the atomic distances. The coordination number is dependent on the choice of integration limit in the profile. In this study, as
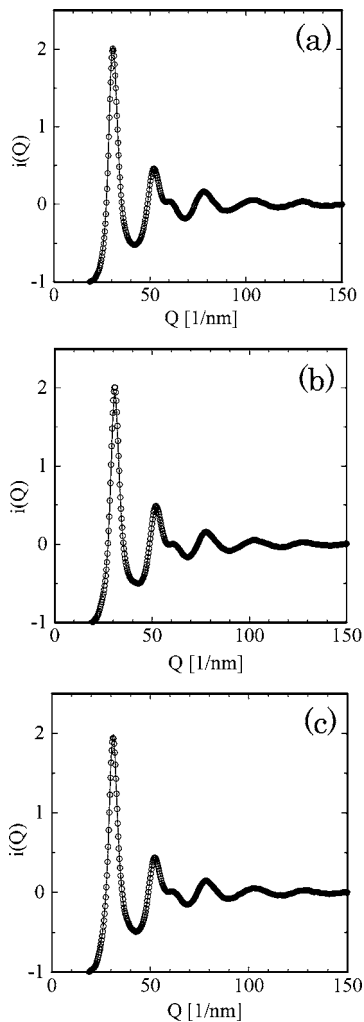
FIG. 5. Interference functions (solid lines) obtained from electron diffraction intensity analyses for as-formed $Fe_{86}B_{14}$ (a), $Fe_{83}B_{17}$ (b), and $Fe_{80}B_{20}$ (c), and are compared with those of calculated functions (open circles) using the RMC simulation.

is often used, the integrations were performed in every three specimens up to the minimum point between the first and the second peaks of their partial PDF profiles along the radial distance; integrations up to 0.35 and 0.30 nm were made for Fe-Fe and Fe-B peaks, respectively. It was found that there is an appreciable increase of Fe-B and B-Fe coordination numbers with the B content. In Table I, radial distances and coordination numbers for Fe-Fe, Fe-B, and B-Fe correlations obtained from neutron and x-ray diffraction study[6] are listed for a-$Fe_{80}B_{20}$ alloy as a reference; their integration limits were 0.345 and 0.255 for Fe-Fe and Fe-B correlation peaks, respectively. According to the present PDF analysis data in Table I, the local chemical order with B-centered trigonal prism with three capping atoms[10] is judged to be almost realized and the nine-coordinated prisms are thought to be increased with the increase of B content. With respect to the circumstance structure for Fe, closely packed atomic arrangements are thought to be realized in appearance, because of the coordination number obtained was nearly 12 in every specimen. The coordination number is almost consistent with other structure analysis data.[5,6,8] On the other hand, accord-
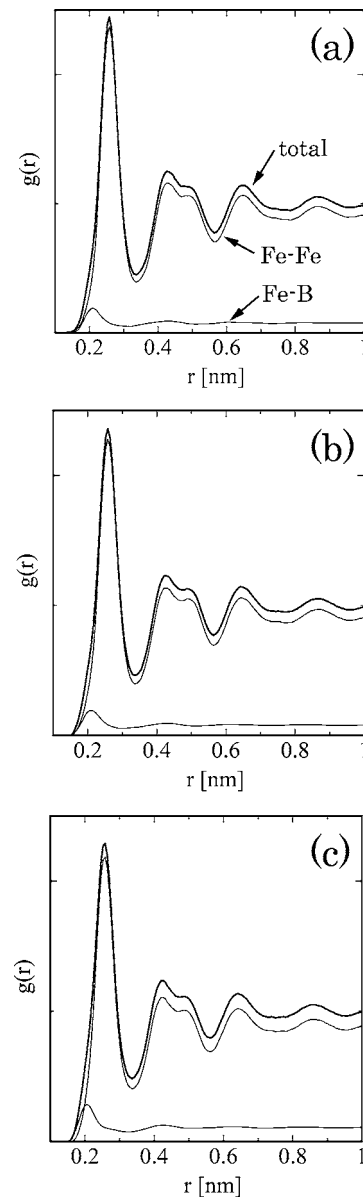

FIG. 6. Atomic pair distribution functions for as-formed $Fe_{86}B_{14}$ (a), $Fe_{83}B_{17}$ (b), and $Fe_{80}B_{20}$ (c). The thick solid lines are of total PDFs, and partial correlation functions for Fe-Fe, Fe-B pairs obtained from RMC simulations are also shown by thin solid lines in these figures.

ing to the Mössbauer spectroscopy and thermomagnetization studies, local bcc-Fe-like atomic configurations have been proposed in amorphous Fe-B alloys with near-eutectic compositions.[13,15] In order to understand amorphous Fe-B structures correctly, a close investigation of the atomic arrangements of Fe atoms is important.

In discussing amorphous alloy structures more in detail, the atomic SRO parameter values using the Cargill-Spaepen parameter[29] is often used. The SRO parameter for an amorphous Fe-B alloy can be expressed as $\eta_{FeB}=Z_{FeB}/Z_{FeB}^*-1$, where Z_{FeB} is the experimental number of B atoms around an Fe atom and Z_{FeB}^* the number of B atoms around Fe for statistical distribution of atoms with $Z_{FeB}^*=c_B Z_B Z_{Fe}/(c_{Fe} Z_{Fe}+c_B Z_B)$. Z_B and Z_{Fe} are total coordination numbers (CNs)

TABLE I. Atomic distances and coordination numbers obtained from the present RMC simulations for the experimental PDFs for a-Fe$_{100-x}$B$_x$ structures. X-ray neutron diffraction data (Ref. 6) are also listed for comparison.

		Fe$_{86B14}$	Fe$_{83}$B$_{17}$	Fe$_{80}$B$_{20}$	Fe$_{80}$B$_{20}$[a]
Fe-B	$r=0.210$ (nm)	0.210	0.206	(0.214)
	$Z=1.5$	1.9	2.4	(2.16)
B-Fe	$r=0.210$ (nm)	0.210	0.206	(0.214)
	9.5	9.4	9.3	(8.64)
Fe-Fe	$r=0.258$ (nm)	0.258	0.257	(0.257)
	12.3	12.2	11.8	(12.4)

[a]Nold *et al.* (Ref. 6).

around B and Fe atoms, respectively. c_B and c_{Fe} are atomic concentrations for B and Fe. η is 0 for statistical distribution, $\eta < 0$ for a segregation tendency, and $\eta > 0$ for a compound forming tendency. According to Table I, the values of η_{FeB} can be evaluated as $\eta_{FeB}=0.09$, 0.14, and 0.18 for a-Fe$_{86}$B$_{14}$, a-Fe$_{83}$B$_{17}$, and a-Fe$_{80}$B$_{20}$ structures, respectively. Needless to say, there are errors in the parameters (coordination numbers) used in calculating the η_{FeB} values. To examine the uncertainties, we constructed three different RMC simulated models for all the three alloys. As a result, the errors for all the η_{FeB} values are found to be within a range of 0.04. All the η_{FeB} values are considered to have positive η_{FeB} values. The positive values mean the tendency of a compound formation, and the tendency increases reasonably as the B composition increases.

C. Structures with nanoscale phase separation

The Voronoi polyhedral analysis has been performed using the three RMC-simulated structure models with different compositions. Figures 7(a)–7(c) show the types of local polyhedral structures surrounding B atoms analyzed for a-Fe$_{86}$B$_{14}$, a-Fe$_{83}$B$_{17}$, and a-Fe$_{80}$B$_{20}$, respectively. In the figure, types of polyhedra, expressed by the Voronoi indices, and their fractions found for central B atoms are shown. It is noted that in each amorphous structure such polyhedral structures as nine-coordinated trigonal prisms (three-capped trigonal prisms) and ten-coordinated Archimedian antiprisms are predominant (the atomic structures are schematically drawn in the figure). Other Voronoi polyhedra with indices such as (044100), (133200), and (036100) all belong to neighboring deformed prism structures. The observed results of prism-related local structures of these a-Fe-B are consistent with the SRO (or chemical order) structures investigated by neutron and x-ray diffraction so far.[6] It should be noted that the typical prism structures, (036000) and (044000), increase in observation frequency as the B composition increases. We obtained the B-Fe correlation numbers (Table I) for these alloys on the basis of experimental structural data analyzed using RMC simulations. The B-Fe correlation numbers obtained are 9.5, 9.4, and 9.3, which increase with the B composition.

Also shown in Figs. 8(a)–8(c) are types of local polyhedral structures surrounding Fe atoms. The index (036400) corresponds to the polyhedral structure of deformed bcc as shown schematically in Fig. 6(b). We also find the index (00 12 000) in each structure, typical of icosahedral cluster. According to a structural simulation study for a-Fe-B, Stepanyuk *et al.*[30] found several Voronoi polyhedra with pentagonal dominance corresponding to the polyhedral structures of deformed bcc or deformed icosahedron. Polyhedral structures with indices (036400), (046400), (036500), (036300), and (028400) are those of deformed bcc clusters, and structures with indices (01 10 200) and (028200) are closer to the icosahedral one. The atomic CN surrounding the central Fe atom, therefore, becomes always more than 12 in each polyhedron. According to the polyhedral analyses, the averaged CN values with the central Fe atom for a-Fe$_{86}$B$_{14}$, a-Fe$_{83}$B$_{17}$, and a-Fe$_{80}$B$_{20}$ are 13.9, 14.1, and 14.2, respectively. On the other hand, according to Table I, the Fe-Fe

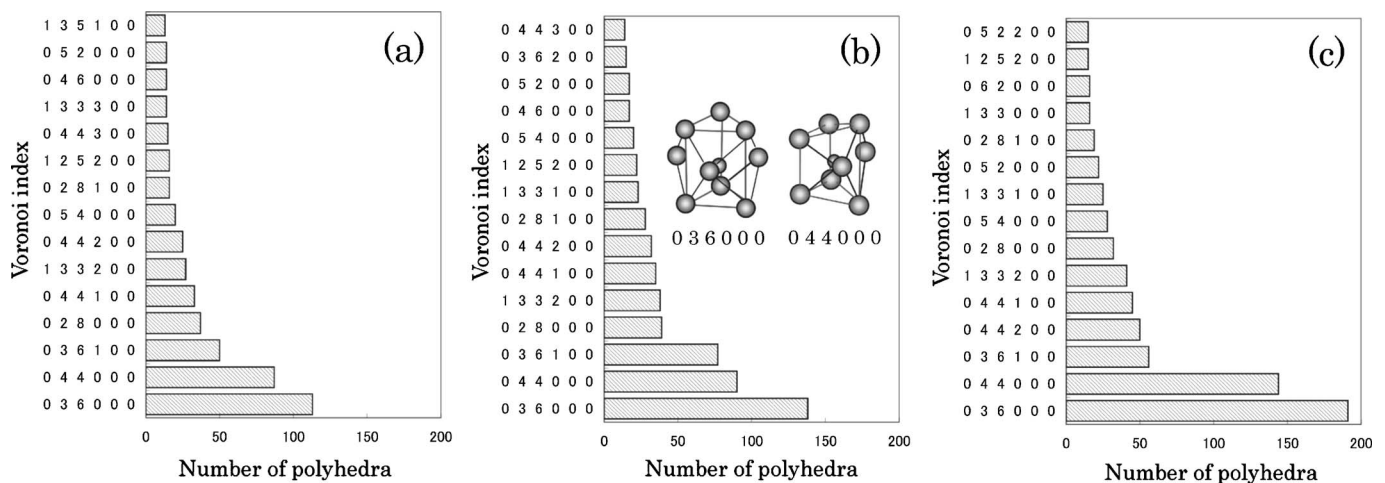FIG. 7. Frequency histograms of B-centered Voronoi polyhedra in the RMC-simulated a-Fe$_{86}$B$_{14}$ (a), a-Fe$_{83}$B$_{17}$ (b), and a-Fe$_{80}$B$_{20}$ (c) structure models. Atomic arrangements of Archimedian antiprism (044000) and nine-coordinated trigonal prism (036000) structures are schematically drawn in (b).
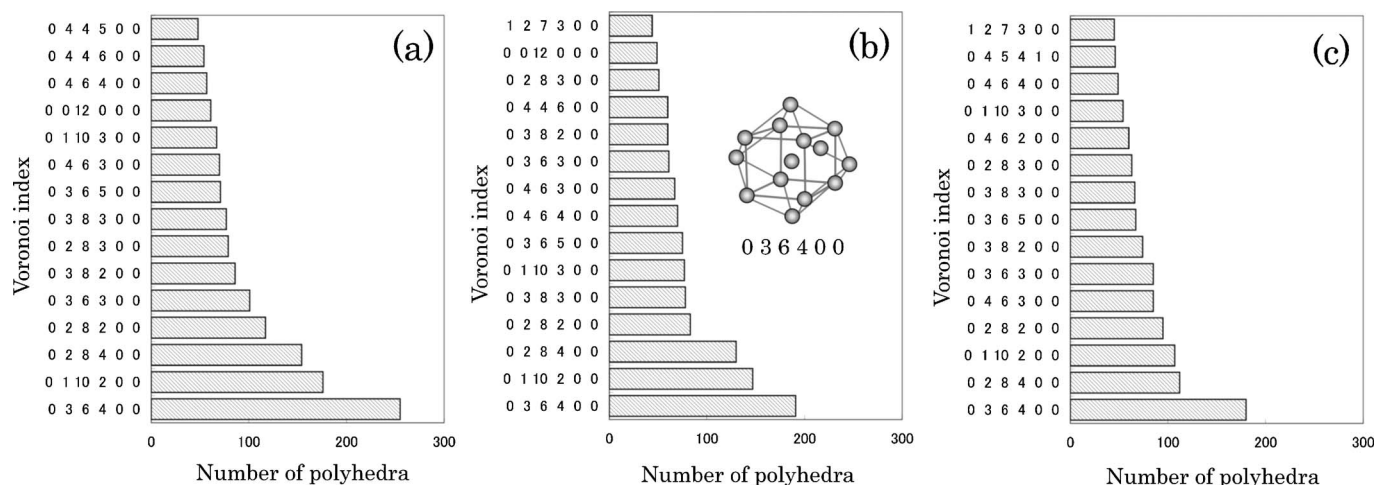
FIG. 8. Frequency histograms of Fe-centered Voronoi polyhedra in the RMC-simulated a-$Fe_{86}B_{14}$ (a), a-$Fe_{83}B_{17}$ (b), and a-$Fe_{80}B_{20}$ (c) structure models. Atomic arrangement of deformed-bcc (036400) is schematically drawn in (b).

correlation number is always close to 12 in the three specimens. The difference between the average CN and the Fe-Fe correlation number surrounding the central Fe atom for each specimen can be attributed to the B occupation in the near-neighbor shells with the central Fe. Assuming a statistical distribution of B on these Fe-centered polyhedra, we find that there are 1.5, 1.9, and 2.4 B atoms in average occupying the polyhedral atomic sites for a-$Fe_{86}B_{14}$, a-$Fe_{83}B_{17}$, and a-$Fe_{80}B_{20}$, respectively. These values changing with the B concentrations are roughly consistent with the Z_{Fe-B} values in Table I. The coordination numbers of about 12 are found in every specimen for Fe-Fe correlation in Table I. The correlation number close to 12 does not necessarily mean that the Fe atoms in these alloys form atomic clusters with 12-coordinated closed packed structures such as fcc-Fe and icosahedral-Fe clusters. This is simply attributed to the fact that the correlation numbers were calculated from the PDF Fe-Fe correlation profile with a wide radial distances ranging between about 0.20 and 0.35 nm in PDF, and a rather relaxed coordination shells with larger coordination numbers are found with deformed-bcc or icosahedra. According to Fig. 8, a formation tendency of deformed-bcc clusters decreases with the decrease of Fe composition. It is interesting that the icosahedral type clusters also decrease with the decrease of Fe composition. Such a decrease of bcc-like or icosahedral-like Fe clusters with the B composition must be correlated to the increase of prism-type atomic clusters with B composition as shown in Fig. 7.

Coexistence of local bcc-Fe-like structures and B-centered trigonal prism structures with strong chemical order has been demonstrated in the present Voronoi polyhedral analysis for the RMC-simulated a-Fe-B structures, together with the compositional changes in their observation frequencies. The above local structure investigation for averaged structures is in good agreement with the local structure observation by HREM and NBED (in Figs. 2 and 3). The results are also consistent with a study by Cunat *et al.*,[15] who

calculated the enthalpy for crystallization and concluded that a mixture of microphases of α-Fe and iron-boride is realized within the range of composition of $x \leq 20$ for a-$Fe_{100-x}B_x$. It can be said that the nanoscale phase separation occurs in as-formed Fe-B glasses near the eutectic composition as a local structure mode to decrease the free-energy of the system attaining a "quenched-in pseudo-phase equilibrium" of eutectic amorphous alloys.

Local structural or compositional fluctuations can be detected when a precise small-angle scattering experiment is performed. Local compositional fluctuations with fluctuation wavelengths as small as $1-2$ nm were studied in the TM-M systems by small-angle scattering.[4,31] Such compositional fluctuation data must be deeply concerned with a local structural fluctuation detected in the present study. More comprehensive studies are necessary to understand the real atomic structures of amorphous alloys in detail.

IV. CONCLUSION

In this study, local structure analysis of as-formed amorphous $Fe_{86}B_{14}$, $Fe_{83}B_{17}$, and $Fe_{80}B_{20}$ alloys were performed comprehensively using HREM, NBED, and electron diffraction structure analysis. Images of atomic clusters corresponding to the bcc-Fe structure were observed locally by HREM in these three specimens. NBED clearly revealed the existence of local Fe-boride clusters together with the local clusters of bcc-Fe(B) in all these specimens. The Voronoi polyhedral analysis of structure models made by RMC simulation using the experimental interference functions showed that atomic arrangements of bcc-Fe-like clusters and trigonal prisms with Fe and B are formed in these a-Fe-B alloys, and their fraction tends to be changed in accordance with the B concentration change. These experimental results demonstrate that the nanoscale phase separation occurs in the a-Fe-B alloys with near-eutectic compositions in such a way

that the phase valance for their primary crystallization is realized approximately down on nanometer scale already in the as-formed state. From the present results, it is concluded that the structure concept of nanoscale phase separation (decomposition) is a realistic one for the eutectic TM-M glass systems.

*Author to whom correspondence should be addressed. Electronic address: ahirata@sanken.osaka-u.ac.jp

†Present address: National Institute for Materials Science, Tsukuba 305-0047, Japan.

[1] A. Inoue, Acta Mater. **48**, 279 (2000).

[2] W. H. Wang, C. Dong, and C. H. Shek, Mater. Sci. Eng., R. **44**, 45 (2004).

[3] N. Mattern, U. Kuhn, H. Hermann, H. Ehrenberg, J. Neuefeind, and J. Eckert, Acta Mater. **50**, 305 (2002).

[4] J. F. Sadoc and J. Dixmier, Mater. Sci. Eng. **23**, 187 (1976).

[5] Y. Waseda, *The Structure of Non-Crystalline Materials, Liquids and Amorphous Solids* (McGraw-Hill, New York, 1980), p. 87.

[6] E. Nold, P. Lamparter, H. Olbrich, G. Rainer-Harbach, and S. Steeb, Z. Naturforsch. A **36A**, 1032 (1981).

[7] T. Fukunaga and K. Suzuki, Sci. Rep. Res. Inst. Tohoku Univ. A **29**, 153 (1981).

[8] T. Fukunaga, M. Misawa, K. Fukamichi, T. Masumoto, and K. Suzuki, *Proceedings Rapidly Quenched Metals V*, edited by S. Steeb and H. Warlimont (North-Holland, Amsterdam, 1985), p. 325.

[9] S. R. Elliott, *Physics of Amorphous Materials* (John Wiley & Sons, New York, 1990), p. 71.

[10] P. H. Gaskell, J. Non-Cryst. Solids **75**, 329 (1985).

[11] T. Hamada and F. E. Fujita, *Proceedings Rapidly Quenched Metals IV* (Japan. Inst. Met., Sendai, 1981), Vol. 1.1, p. 319; Jpn. J. Appl. Phys., Part 1 Part 1, **25**, 318 (1986).

[12] J. M. Dubois and G. Le Caer, J. Phys. Colloq. **43**, 67 (1982).

[13] R. Ohshima and F. E. Fujita, Jpn. J. Appl. Phys. **20**, 1 (1981).

[14] R. Hasegawa and R. Ray, J. Appl. Phys. **50**, 1586 (1979).

[15] C. Cunat, M. Notin, M. Herz, J. Dubois, and G. Le Caer, J. Non-Cryst. Solids **55**, 45 (1983).

[16] Y. Hirotsu and R. Akada, Jpn. J. Appl. Phys., Part 2 **23**, 478 (1984).

[17] Y. Hirotsu, M. Uehara, and M. Ueno, J. Appl. Phys. **59**, 3081 (1986).

[18] K. Anazawa, Y. Hirotsu, and Y. Inoue, Acta Metall. Mater. **42**, 1997 (1994).

[19] Y. Hirotsu, T. Ohkubo, and M. Matsushita, Microsc. Res. Tech. **40**, 284 (1998).

[20] T. Ohkubo and Y. Hirotsu, Phys. Rev. B **67**, 094201 (2003).

[21] Y. Zhang, K. Hono, A. Inoue, A. Makino, and T. Sakurai, Acta Mater. **44**, 1497 (1996).

[22] W. Sinkler, C. Michaelsen, and R. Bormann, J. Mater. Res. **12**, 872 (1997).

[23] R. McGreevy and L. Pusztal, Mol. Simul. **1**, 359 (1988).

[24] R. McGreevy, J. Phys.: Condens. Matter **13**, R877 (2001).

[25] N. E. Cusack, *The Physics of Structurally Disordered Matter* (Institute of Physics Pub., Inc., 1987), p. 26.

[26] Available at http://www.cristal.org/

[27] J. M. Cowley, *Diffraction Physics* (North-Holland, Amsterdam, 1981), Chap. 11.

[28] J. M. Zuo and J. C. H. Spence, Philos. Mag. A **68**, 1055 (1993).

[29] G. S. Cargill III and F. Spaepen, J. Non-Cryst. Solids **43**, 91 (1981).

[30] V. S. Stepanyuk, A. Szasz, A. A. Katsnelson, O. S. Trushin, H. Muller, and H. Kirchmayr, J. Non-Cryst. Solids **159**, 80 (1993).

[31] E. Nold, S. Steeb, and P. Lamparter, Z. Naturforsch. A **35A**, 610 (1980).